Faculty Publications   Astronomy

2011

The Atacama Cosmology Telescope: Sunyaev-Zel'Dovich Selected Galaxy Clusters at 148 Ghz in the 2008 Survey

Tobias A. Marriage

Viviana Acquaviva

Peter A. R. Ade

Bruce Partridge
Haverford College, bpartrid@haverford.edu

Follow this and additional works at: https://scholarship.haverford.edu/astronomy_facpubs

2011

The Atacama Cosmology Telescope: Sunyaev-Zel'Dovich Selected Galaxy Clusters at 148 Ghz in the 2008 Survey

Tobias A. Marriage

Viviana Acquaviva

Peter A. R. Ade

R. Bruce Partridge
Haverford College

THE ATACAMA COSMOLOGY TELESCOPE: SUNYAEV–ZEL'DOVICH-SELECTED GALAXY CLUSTERS AT 148 GHz IN THE 2008 SURVEY

Tobias A. Marriage[1,32], Viviana Acquaviva[1,2], Peter A. R. Ade[3], Paula Aguirre[4], Mandana Amiri[5],
John William Appel[6], L. Felipe Barrientos[4], Elia S. Battistelli[5,7], J. Richard Bond[8], Ben Brown[9], Bryce Burger[5],
Jay Chervenak[10], Sudeep Das[1,6,11], Mark J. Devlin[12], Simon R. Dicker[12], W. Bertrand Doriese[13], Joanna Dunkley[1,6,14],
Rolando Dünner[4], Thomas Essinger-Hileman[6], Ryan P. Fisher[6], Joseph W. Fowler[6,13], Amir Hajian[1,6,8],
Mark Halpern[5], Matthew Hasselfield[5], Carlos Hernández-Monteagudo[15], Gene C. Hilton[13], Matt Hilton[16,17],
Adam D. Hincks[6], Renée Hlozek[14], Kevin M. Huffenberger[18], David Handel Hughes[19], John P. Hughes[2],
Leopoldo Infante[4], Kent D. Irwin[13], Jean Baptiste Juin[4], Madhuri Kaul[12], Jeff Klein[12], Arthur Kosowsky[9],
Judy M. Lau[6,20,21], Michele Limon[6,12,22], Yen-Ting Lin[1,4,23], Robert H. Lupton[1], Danica Marsden[12],
Krista Martocci[6,24], Phil Mauskopf[3], Felipe Menanteau[2], Kavilan Moodley[16,17], Harvey Moseley[10],
Calvin B. Netterfield[25], Michael D. Niemack[6,13], Michael R. Nolta[8], Lyman A. Page[6], Lucas Parker[6],
Bruce Partridge[26], Hernan Quintana[4], Erik D. Reese[12], Beth Reid[6,27], Neelima Sehgal[20], Blake D. Sherwin[6],
Jon Sievers[8], David N. Spergel[1], Suzanne T. Staggs[6], Daniel S. Swetz[12,13], Eric R. Switzer[6,25], Robert Thornton[12,28],
Hy Trac[29,30], Carole Tucker[3], Ryan Warne[16], Grant Wilson[31], Ed Wollack[10], and Yue Zhao[6]

[1] Department of Astrophysical Sciences, Peyton Hall, Princeton University, Princeton, NJ 08544, USA
[2] Department of Physics and Astronomy, Rutgers, The State University of New Jersey, Piscataway, NJ 08854-8019, USA
[3] School of Physics and Astronomy, Cardiff University, The Parade, Cardiff, Wales CF24 3AA, UK
[4] Departamento de Astronomía y Astrofísica, Facultad de Física, Pontificía Universidad Católica, Casilla 306, Santiago 22, Chile
[5] Department of Physics and Astronomy, University of British Columbia, Vancouver, BC V6T 1Z4, Canada
[6] Joseph Henry Laboratories of Physics, Jadwin Hall, Princeton University, Princeton, NJ 08544, USA
[7] Department of Physics, University of Rome "La Sapienza," Piazzale Aldo Moro 5, I-00185 Rome, Italy
[8] Canadian Institute for Theoretical Astrophysics, University of Toronto, Toronto, ON M5S 3H8, Canada
[9] Department of Physics and Astronomy, University of Pittsburgh, Pittsburgh, PA 15260, USA
[10] Code 553/665, NASA/Goddard Space Flight Center, Greenbelt, MD 20771, USA
[11] Berkeley Center for Cosmological Physics, LBL and Department of Physics, University of California, Berkeley, CA 94720, USA
[12] Department of Physics and Astronomy, University of Pennsylvania, Philadelphia, PA 19104, USA
[13] NIST Quantum Devices Group, Boulder, CO 80305, USA
[14] Department of Astrophysics, Oxford University, Oxford OX1 3RH, UK
[15] Max Planck Institut für Astrophysik, Postfach 1317, D-85741 Garching bei München, Germany
[16] Astrophysics and Cosmology Research Unit, School of Mathematical Sciences, University of KwaZulu-Natal, Durban 4041, South Africa
[17] Centre for High Performance Computing, CSIR Campus, Rosebank, Cape Town, South Africa
[18] Department of Physics, University of Miami, Coral Gables, FL 33124, USA
[19] Instituto Nacional de Astrofísica, Óptica y Electrónica (INAOE), Tonantzintla, Puebla, Mexico
[20] Kavli Institute for Particle Astrophysics and Cosmology, Stanford University, Stanford, CA 94305-4085, USA
[21] Department of Physics, Stanford University, Stanford, CA 94305-4085, USA
[22] Columbia Astrophysics Laboratory, New York, NY 10027, USA
[23] Institute for the Physics and Mathematics of the Universe, The University of Tokyo, Kashiwa, Chiba 277-8568, Japan
[24] Kavli Institute for Cosmological Physics, Chicago, IL 60637, USA
[25] Department of Physics, University of Toronto, Toronto, ON M5S 1A7, Canada
[26] Department of Physics and Astronomy, Haverford College, Haverford, PA 19041, USA
[27] Institut de Ciencies del Cosmos (ICC), University of Barcelona, Barcelona 08028, Spain
[28] Department of Physics, West Chester University of Pennsylvania, West Chester, PA 19383, USA
[29] Department of Physics, Carnegie Mellon University, Pittsburgh, PA 15213, USA
[30] Harvard-Smithsonian Center for Astrophysics, Harvard University, Cambridge, MA 02138, USA
[31] Department of Astronomy, University of Massachusetts, Amherst, MA 01003, USA

ABSTRACT

We report on 23 clusters detected blindly as Sunyaev–Zel'dovich (SZ) decrements in a 148 GHz, 455 deg^2 map of the southern sky made with data from the Atacama Cosmology Telescope 2008 observing season. All SZ detections announced in this work have confirmed optical counterparts. Ten of the clusters are new discoveries. One newly discovered cluster, ACT-CL J0102−4915, with a redshift of 0.75 (photometric), has an SZ decrement comparable to the most massive systems at lower redshifts. Simulations of the cluster recovery method reproduce the sample purity measured by optical follow-up. In particular, for clusters detected with a signal-to-noise ratio greater than six, simulations are consistent with optical follow-up that demonstrated this subsample is 100% pure. The simulations further imply that the total sample is 80% complete for clusters with mass in excess of 6×10^{14} solar masses referenced to the cluster volume characterized by 500 times the critical density. The Compton y–X-ray luminosity mass comparison for the 11 best-detected clusters visually agrees with both self-similar and non-adiabatic, simulation-derived scaling laws.

Key words: cosmic background radiation – cosmology: observations – galaxies: clusters: general – radio continuum: general – surveys

1. INTRODUCTION

Measuring the redshift evolution of the mass function of galaxy clusters provides powerful constraints on cosmological parameters, complementary to those obtained from different measurements, such as the angular power spectrum of the cosmic microwave background (CMB; e.g., Komatsu et al. 2011) or luminosity distances of Type Ia supernovae (e.g., Hicken et al. 2009). The potential of cluster surveys as a cosmological probe has recently been demonstrated through the analysis of large X-ray and optically selected cluster samples spanning a wide range in redshift (e.g., Vikhlinin et al. 2009; Mantz et al. 2010; Rozo et al. 2010).

A powerful method for cluster detection and characterization is provided by the thermal Sunyaev–Zel'dovich (SZ) effect. The SZ effect is the process by which energy is transferred from the hot intracluster medium (ICM) of galaxy clusters to the CMB through inverse Compton scattering (Zel'dovich & Sunyaev 1969; Sunyaev & Zel'dovich 1970). The overall effect is to distort the thermal spectrum of the CMB. In the case of the present study at 148 GHz, the SZ distortion produces a roughly arcminute-scale temperature decrement along the line of sight to a galaxy cluster. The SZ distortion is proportional to the pressure of the ICM integrated along the line of sight, providing a unique probe of cluster physics. The integrated SZ flux therefore scales as the thermal energy content of the cluster, which is expected to scale with cluster mass for cluster gas hydrostatically supported by thermal pressure. The amplitude of the SZ distortion is approximately independent of the cluster redshift, in marked contrast to the observed cluster brightness in other wave bands. Therefore, the SZ effect is particularly suited for inventorying the distant universe. Galaxy cluster surveys are one of the few methods that probe the growth of structure and the interpretation of survey yields has the potential to precisely constrain the equation of state of dark energy (e.g., Bartlett & Silk 1994; Holder et al. 2000; Haiman et al. 2001; Majumdar & Mohr 2004). For a full description of the SZ effect, historical perspectives, and applications to cosmology, see the review articles by Bernstein & Dodelson (1990), Birkinshaw (1991), Rephaeli (1995), Birkinshaw (1999), and Carlstrom et al. (2002).

The history of successful targeted observations of the SZ effect in previously known galaxy clusters goes back two decades. Pioneering measurements were made with the Owens Valley Radio Observatory (OVRO) 40 m telescope (Birkinshaw et al. 1991), the Ryle Telescope (Jones et al. 1993), the OVRO 5 m telescope (Herbig et al. 1995; Myers et al. 1997), the OVRO/BIMA interferometers (Carlstrom et al. 1996), the bolometric SUZIE receiver on the Caltech Submillimeter Observatory (Holzapfel et al. 1997), and the Nobeyama Radio Observatory 45 m telescope (Komatsu et al. 1999). Scientifically these original studies put special emphasis on deriving the Hubble parameter from angular diameter distances to clusters measured through a combination of SZ and X-ray data. In the last decade, these geometric measurements have been expanded to statistically significant samples of clusters (e.g., the OVRO/BIMA studies by Reese et al. 2002 and Bonamente et al. 2006) and serve as an independent check on estimates that rely on the conventional extragalactic distance ladder (e.g., Freedman et al. 2001; Riess et al. 2009). Beyond distance scale studies, targeted SZ work has focused on understanding the SZ correlation to

other cluster observables, especially those which trace mass (e.g., Benson et al. 2004; Bonamente et al. 2008; McInnes et al. 2009; Marrone et al. 2009; Melin et al. 2011; Huang et al. 2010; Plagge et al. 2010; Culverhouse et al. 2010). The SZ/X-ray and SZ/optical lensing correlations provide the mass calibration necessary for understanding the cluster mass function through cosmic time. By measuring the redshift evolution of the cluster mass function, constraints can be put on the matter density field and dark energy. Thus, proper mass calibration is essential for studying cosmology with clusters (e.g., Francis et al. 2005). Finally, targeted SZ observations are expanding our knowledge of the physics of the ICM by probing the cluster gas pressure at large radius (Mroczkowski et al. 2009; Plagge et al. 2010; Komatsu et al. 2011) as well as at high resolution (Komatsu et al. 2001; Mason et al. 2010).

The first blind detections of galaxy clusters through their SZ effect were reported by Staniszewski et al. (2009) for the South Pole Telescope (SPT; Carlstrom et al. 2011). Three of the clusters from Staniszewski et al. (2009) were previously unknown. Hincks et al. (2010) reported on the cluster detections for the Atacama Cosmology Telescope (ACT; Fowler et al. 2007; Swetz et al. 2011). While the clusters from Hincks et al. (2010) were previously known, they were blindly detected in the survey data. SPT and ACT have been able to realize blind detections from cosmologically significant surveys because they combine three essential design features: arcminute resolution matched to the size of clusters, degree-scale fields of view for efficient surveying, and the unprecedented sensitivity of 1000 element bolometric detector arrays. In Vanderlinde et al. (2010), the SPT collaboration reported on 21 cluster candidates, 20 of which were optically confirmed (High et al. 2010). In a follow-up study, Andersson et al. (2011) presented the X-ray properties of the SPT sample and derived SZ/X-ray correlations. Furthermore, Vanderlinde et al. (2010) obtained cosmological constraints from an SZ-selected sample of clusters.

In this work, the ACT collaboration reports on 23 clusters detected in a subset of the data taken during the 2008 observing season. This paper describes the detection and millimeter properties of the clusters. Companion papers describe the physical properties and observed purity of the cluster sample (Menanteau et al. 2010) as well as cosmological implications (Sehgal et al. 2011). These papers and others cited above are part of a larger initial science release from ACT, which also includes results on the CMB power spectrum and associated parameter constraints (Fowler et al. 2010; Das et al. 2011; Dunkley et al. 2011; Hajian et al. 2011) and on compact millimeter sources (Marriage et al. 2011).

This paper is organized as follows. The data reduction and catalog construction are described in Section 2. The detections and their properties are discussed in Section 3. An estimate of purity and completeness of the sample is derived from simulations in Section 4. Finally, in Section 5, the SZ signal is compared to X-ray-derived mass for a high-significance subset of the cluster sample.

2. FROM OBSERVATIONS TO CLUSTER DETECTION

The observations and methods to reduce the raw data to maps for this work are the same as those used in the 2008 power spectrum study (Fowler et al. 2010) and extragalactic source study (Marriage et al. 2011). The primary difference between the source and cluster study lies in the compact signal profile used in the implementation of the matched filter-based detection. Therefore, we restrict our discussion here to a short summary of the
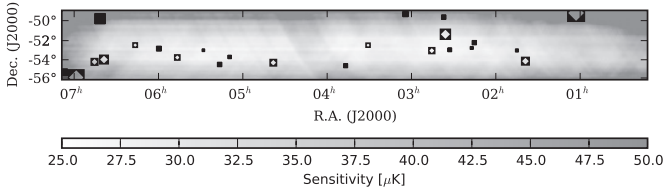
Figure 1. Sensitivity map with detections. The map shows the sensitivity over the subset of the ACT 2008 148 GHz data set considered for this study. The gray scale encodes the noise rms in μK of a map match-filtered for a β-model ($\beta = 0.86$, $\theta_c = 1\rlap{.}'00$). The median noise in the map is $36\,\mu$K. Black boxes mark the location of the 23 optically confirmed clusters. The size of each box is proportional to the corresponding cluster decrement.

observations and data reduction, and refer the reader to Fowler et al. (2010) and Marriage et al. (2011) for a more complete description. We describe in detail the particular implementation of the matched filter for clusters. For a description of the ACT receiver and instrumentation see Swetz et al. (2011).

2.1. Observations and Data Reduction

ACT is a 6 m telescope operating at 5200 m in the Atacama Desert of northern Chile. The site was chosen for its excellent atmospheric transparency and access to both southern and northern skies. The telescope has three 1024 element arrays of transition edge sensors operating at 148 GHz, 218 GHz, and 277 GHz. This study uses 148 GHz data from a 455 deg^2 subregion of the 2008 southern survey. The subregion lies between right ascensions 00^h12^m and 07^h08^m and declinations $-56°11'$ and $-49°00'$. Figure 1 is a map of the sensitivity across the subregion along with the locations of the clusters reported in this study. The median rms of the map optimally filtered for detecting a β-model profile ($\beta = 0.86$, $\theta_c = 1\rlap{.}'00$) is $36\,\mu$K.

The data for this study were calibrated to the temperature of Uranus with a precision of 6%. The absolute positional uncertainty in the maps is established at $3\rlap{.}''5$ by comparison of ACT radio source locations (Marriage et al. 2011) to cross-identified sources in the Australia Telescope 20 GHz Survey (Murphy et al. 2010). Note, however, that reported cluster locations have an additional uncertainty due to the effect of noise on the estimate of the cluster center. Considering the positional uncertainty for sources detected between signal-to-noise ratios (S/Ns) 5.5 and 10 reported in Marriage et al. (2011), we expect estimates of the ACT cluster center positions to scatter with an rms of roughly $10''$. Additional ambiguity in the cluster position arises in the case of an extended, non-spherical (e.g., disturbed) system. In such cases, the positional uncertainty can rise to arcminute scales.

With calibration and astrometry solved, the final step in the data reduction is map making. We iteratively solve for the maximum likelihood (ML) estimate of the map using a custom preconditioned conjugate gradient code (e.g., Press et al. 1992). Because ACT samples the sky along multiple scan directions (i.e., the data are cross-linked), we are able to produce an unbiased ML map of the microwave sky with a faithful representation of structure from degree to arcminute scales.

2.2. Filtering and Cluster Extraction

For cluster detection we use matched filters (Haehnelt & Tegmark 1996; Herranz et al. 2002; Melin et al. 2006). We model the sky temperature fluctuation at a point $\boldsymbol{x}$ as

$$\delta T(\boldsymbol{x}) = \sum_i \delta T_{0,i} B_{\theta_c,i}(\boldsymbol{x} - \boldsymbol{x}_i) + \delta T_{\text{other}}(\boldsymbol{x}), \qquad (1)$$
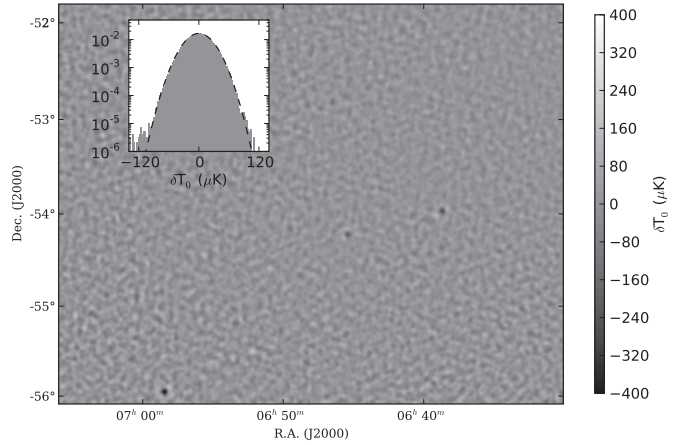
Figure 2. 148 GHz sub-map. The data have been weighted by a smooth function $\sqrt{N_{\text{obs}}/N_{\text{obs,max}}}$, where N_{obs} is the number of data per pixel. This weighting levels the amplitude of white noise across the map to that corresponding to the deepest data. The data are then match-filtered with a β-profile ($\theta_c = 1\rlap{.}'0$). The coverage becomes shallower toward the bottom left of the map, causing a visible increase in the rms. The inset shows the flux density distribution across the data weighted by the square root of the number of data per pixel. The data distribution is shown as a gray histogram on which a dashed Gaussian distribution with standard deviation $24\,\mu$K is plotted. Sources were removed prior to filtering. Three clusters are recognizable from left to right: the Bullet Cluster (bottom left), A3404 (middle), and AS0592 (middle right).

where $\delta T_{0,i}$ and $B_{\theta_c,i}$ are the amplitude and unit-normalized profile of the ith cluster. In what follows we choose B_{θ_c} to be the isothermal β-model ($\beta = 0.86$) with core radius θ_c ranging from $0\rlap{.}'25$ to $4\rlap{.}'0$ and convolved with an isotropic ACT 148 GHz beam from Hincks et al. (2010). The profile is tapered to zero by multiplication with a cosine in the range 0.5–$5.5\theta_c$. The choice of β is motivated by the best fit to an average SZ profile in Plagge et al. (2010) who found consistency between the β-model fit and the generalized Navarro–Frenk–White profile fit to Y_X in Arnaud et al. (2010). The temperature field $\delta T_{\text{other}}(\boldsymbol{x})$ consists of noise modeled from difference maps, primordial CMB fluctuations with power spectrum from Nolta et al. (2009), as well as sources and undetectable (i.e., low-mass) clusters. The spectral signature of the source and cluster contribution to $\delta T_{\text{other}}(\boldsymbol{x})$ is modeled from fits to ACT data in Fowler et al. (2010). See Marriage et al. (2011) for a full discussion of $\delta T_{\text{other}}(\boldsymbol{x})$.

Before filtering, bright (S/N > 5) sources are in-painted with sky temperature in the neighborhood of the source. Furthermore, the map is weighted by the inverse square root of the number of observations. This has the effect of flattening the white noise across the map. The map is filtered in the Fourier domain using a matched filter

$$\delta T_{\text{filt}}(\boldsymbol{k}) = \frac{\widetilde{B}_{\theta_c}^*(\boldsymbol{k})|\widetilde{\delta T}_{\text{other}}(\boldsymbol{k})|^{-2}\delta T(\boldsymbol{k})}{\int \widetilde{B}_{\theta_c}^*(\boldsymbol{k}')|\widetilde{\delta T}_{\text{other}}(\boldsymbol{k}')|^{-2}\widetilde{B}_{\theta_c}(\boldsymbol{k}')\,d\boldsymbol{k}'}, \qquad (2)$$

where $\widetilde{B}_{\theta_c}(\boldsymbol{k})$ and $\widetilde{\delta T}_{\text{other}}(\boldsymbol{k})$ are the Fourier transforms of B_{θ_c} and δT_{other}, respectively. The map is filtered using β-models with core radii from $0\rlap{.}'25$ to $4\rlap{.}'0$ in $0\rlap{.}'25$ steps. These core radii were chosen to span the range of angular scales characterizing massive clusters from low to high redshift. In a given map, the S/N of a detection is defined as the ratio of the extremum of the cluster decrement to the rms of the filtered map. The reported S/N for a given detection is the maximum S/N from the set of filtered maps. Figure 2 shows a subsection of the source-masked and filtered map containing three known clusters. Shown in an inset of this figure is the pixel flux distribution of the filtered

map. The flux distribution suggests the filtered map is dominated by Gaussian noise.

The filter in Equation (2) is normalized such that the central decrement in the filtered map is an estimate of the central decrement value in μK. It is this value, recovered from the filtered map, which we use as our decrement estimate. As discussed in Marriage et al. (2011), this estimate suffers from increased error and bias due to the 0.″5 pixel size of the ACT maps. In order to mitigate these errors, the pixel size of submaps around each detection is decreased by Fourier transforming the map and adding extra zeros to the boundary of the Fourier transform. The inverse of this zero-padded transform is then the original submap with smaller pixels. For this study, the pixel size is changed to 0.″0625, which reduces the errors associated with the discrete approximation of Equation (2) to less than 1%. The errors we quote for the map-derived decrements are simply the decrement amplitude divided by the S/N.

3. CLUSTER DETECTIONS AND PROPERTIES

Table 1 lists clusters detected by ACT. All detections in the table have been confirmed through optical follow-up imaging of a larger catalog of all SZ candidates from the ACT data (Menanteau et al. 2010). The table is divided into two groups of candidates: candidates detected at S/N > 6 and candidates detected at lesser significance. The optical follow-up showed that for candidates detected at S/N > 6, the larger catalog of all SZ candidates is 100% pure (see also Section 4). Of the nine detections at S/N > 6, three are newly discovered systems. Among the 14 candidates confirmed at lower S/N, seven are new detections. Thumbnails of the cluster decrements are shown in Figure 3.

The multifrequency properties of the clusters covered in this work are discussed at length in Hincks et al. (2010) and Menanteau et al. (2010). Paraphrasing these studies, X-ray luminosities were computed from *Chandra* and *XMM* observations where available and supplemented by the *ROSAT* All Sky Survey for the remaining clusters. These luminosities suggest that the full sample is composed of high-mass clusters with a characteristic mass of $M_{500c} \sim 6 \times 10^{14}\ M_\odot$, where M_{500c} is defined as the mass of the cluster at 500 times the critical density of the universe at the cluster redshift. The sample has a median redshift of 0.44. All but one of the clusters at $z > 0.35$ in the sample were discovered via the SZ.

Of the new ACT clusters, the most notable is ACT-CL J0102−4915. This cluster has a decrement amplitude ($\delta T' = -1046 \pm 116\ \mu$K) comparable to that of the Bullet Cluster ($\delta T' = -734 \pm 64\ \mu$K) as well as a smaller angular core radius, consistent with its higher redshift ($z_{photo} = 0.75$). The X-ray luminosity (0.1–2.4 keV) derived from *ROSAT* observations is $18.39 \pm 6.49 \times 10^{44}\ \mathrm{erg\ s^{-1}}$, which is also comparable to that of the Bullet as well as the other massive clusters in our sample (Menanteau et al. 2010). The cluster richness is also consistent with that of a massive cluster ($N_{gal} \approx 50$). The strength of this decrement may result from merger activity, elongation along the line of sight, or other decrement-enhancing effects. Planned spectroscopic and IR follow-up observations will determine the true nature of the decrement.

Table 1 contains estimates of the cluster decrement amplitudes δT_0 based upon the matched filter described in Section 2.2. Also listed is the core radius θ_c corresponding to the filter that exhibits the largest S/N for each cluster. Figure 4 shows the temperature decrement and S/N of two newly discovered clusters plotted as a function of filter scale (i.e., the core radius). For

some of the clusters, such as ACT-CL J0346−5438 shown in the figure, the S/N is a relatively broad function of core radius. The corresponding uncertainty in the size of the cluster results from the blending of the cluster decrement with the background (e.g., CMB). This confusion for single-frequency data was observed by Melin et al. (2006) as well as Vanderlinde et al. (2010). For clusters with a more compact and pronounced core, like ACT-CL J0102−4915, the cluster-background confusion is smaller and so the optimal filter scale is easier to determine from the data. Confusion with the background inflates θ_c while contamination by detector white noise causes a cluster to appear more compact than it actually is. The latter effect can be explained by the fact that most of the power in the white noise field is at the smallest scales. Simulations (see Section 4) show contamination for clusters detected outside the range $\theta_c = 0.″75$–1.″75. For this reason, θ_c estimates reported below 0.″75 or above 1.″75 are suspect. Incorporation of ACT's multiple frequencies will help distinguish clusters from background. Additional years of data will help reduce the fraction of white-noise-boosted detections.

The δT_0 recovered from the filter is the amplitude of the cluster decrement in the ACT map. As such, it is the amplitude of the intrinsic cluster profile convolved with the ACT beam. In Table 1 we also include an estimate of the decrement $\delta T_0' = \delta T_0 C^{-1}(\theta_c)$ where we have corrected the raw δT_0 by the smearing effect of the beam on the height of the corresponding β-profile. This correction for a β-profile with $\theta_c = 1'$ is 1.67. The correction is larger for smaller core radii. To estimate the uncertainty in the recovered $\delta T_0'$, the cluster extraction algorithm was run on a simulation with realistic ACT noise, CMB, and clusters with symmetric β-model profiles. The more realistic simulations of Sehgal et al. (2010) were not used as they were not provided an estimate of the decrement amplitude. As the β-model profiles in this simulation are matched to our filters, the error estimate from these simulations should be taken as a lower limit. With those caveats, the mean error on $\delta T_0'$ from the simulations is 20% greater than the statistical error inferred from the S/N (i.e., systematic errors are 40% of the total error budget). This modest increase in the error budget was accompanied by a large scatter in recovered scale ($\sim$30% with respect to the input scale value) with a non-Gaussian tail toward larger recovered radii. This implies that while the physical scale of the cluster may be confused with the background, the amplitude of the peak is relatively immune to this confusion. When the cluster extraction algorithm was run on the β-model simulations with prior knowledge of the scale, the resulting scatter in recovered $\delta T_0'$ values was consistent with the statistical error inferred from the S/N. Thus, we infer that, in the ideal case of β-model cluster profiles, uncertainty in scale adds 20% scatter to our uncertainty in $\delta T_0'$. For more realistic cluster profiles (e.g., asymmetric), this scatter should be larger.

Because the cluster counts are a falling function of mass (and therefore of decrement amplitude), clusters detected at low significance are more likely to be lower mass systems with a noise-boosted decrement than a higher mass system with a noise-suppressed decrement. In particular, members of the lower significance (S/N < 6) fraction of the ACT detections are likely to have their $\delta T_0'$ overestimated due to noise boosting. In this work, no correction has been made for this bias. An additional bias arises from optimizing the detection significance over the two celestial coordinates and θ_c. Vanderlinde et al. (2010) show that this latter bias, when referred to S/N, can be

Table 1
ACT 2008 148 GHz SZ-selected Galaxy Clusters

| ACT ID	R.A. (J2000) Decl.		S/N	θ_c	δT_0[a]	$\delta T_0'$[b]	y_0'	z[c]	Alternative ID
	(hms)	(° ′ ″)		(′)	(μK)	(μK)	($\times 10^{-4}$)		
			All Candidates S/N > 6						
ACT-CL J0658−5557	06:58:30	−55:57:04	11.5	1.25	−483 ± 42	−734 ± 64	2.98 ± 0.26	0.30	1E0657-56 (Bullet)
ACT-CL J0638−5358	06:38:46	−53:58:45	10.0	1.25	−278 ± 28	−423 ± 42	1.68 ± 0.17	0.22	AS0592
ACT-CL J0245−5302	02:45:33	−53:02:04	9.1	1.00	−198 ± 22	−336 ± 37	1.32 ± 0.15	0.30	AS0295
ACT-CL J0102−4915	01:02:53	−49:15:19	9.0	0.75	−520 ± 58	−1046 ± 116	4.13 ± 0.46	0.75	New
ACT-CL J0438−5419	04:38:19	−54:19:05	8.0	0.50	−214 ± 27	−596 ± 74	2.35 ± 0.29	0.54	New
ACT-CL J0645−5413	06:45:30	−54:13:39	7.1	0.75	−221 ± 31	−444 ± 63	1.75 ± 0.25	0.17	A3404
ACT-CL J0546−5345	05:46:37	−53:45:32	6.5	1.75	−178 ± 27	−240 ± 37	0.95 ± 0.15	1.07	SPT-CL 0547−5345
ACT-CL J0235−5121	02:35:52	−51:21:16	6.2	4.00	−320 ± 51	−363 ± 58	1.43 ± 0.23	0.43	New
ACT-CL J0330−5227	03:30:54	−52:28:04	6.1	1.25	−145 ± 24	−221 ± 36	0.85 ± 0.14	0.44	A3128 (NE)
			S/N < 6 and Optically Confirmed						
ACT-CL J0616−5227	06:16:36	−52:27:35	5.9	0.50	−155 ± 26	−431 ± 73	1.70 ± 0.29	0.71	New
ACT-CL J0559−5249	05:59:43	−52:49:13	5.1	2.25	−155 ± 31	−194 ± 38	0.77 ± 0.15	0.61	SPT-CL J0559−5249
ACT-CL J0215−5212	02:15:18	−52:12:30	4.9	0.25	−140 ± 29	−801 ± 164	3.16 ± 0.65	0.51	New
ACT-CL J0509−5341	05:09:21	−53:42:05	4.8	0.50	−115 ± 24	−319 ± 67	1.27 ± 0.27	0.46	SPT-CL 0509−5342
ACT-CL J0641−4949	06:41:35	−49:48:32	4.7	0.25	−283 ± 60	−1625 ± 375	6.41 ± 1.48	0.15	A3402
ACT-CL J0232−5257	02:32:45	−52:57:08	4.7	0.25	−124 ± 26	−710 ± 152	2.80 ± 0.60	0.59	New
ACT-CL J0516−5430	05:16:30	−54:30:30	4.6	1.75	−143 ± 31	−192 ± 43	0.77 ± 0.17	0.29	AS0520/SPT-CL 0517−5430
ACT-CL J0346−5438	03:46:51	−54:38:54	4.4	1.25	−131 ± 30	−198 ± 45	0.78 ± 0.18	0.55	New
ACT-CL J0217−5245	02:17:11	−52:45:20	4.1	1.25	−98 ± 24	−150 ± 37	0.59 ± 0.14	0.34	RXC J0217.2−5244
ACT-CL J0145−5301	01:44:59	−53:01:01	4.0	1.00	−99 ± 25	−167 ± 42	0.65 ± 0.16	0.12	A2941
ACT-CL J0237−4939	02:37:03	−49:39:27	3.9	1.00	−140 ± 36	−236 ± 61	0.93 ± 0.24	0.40	New
ACT-CL J0304−4921	03:04:15	−49:21:42	3.9	1.00	−169 ± 43	−285 ± 74	1.12 ± 0.29	0.47	New
ACT-CL J0707−5522	07:07:13	−55:22:48	3.3	1.75	−218 ± 67	−293 ± 90	1.16 ± 0.35	0.43	New
ACT-CL J0528−5259	05:28:03	−52:59:53	3.1	0.50	−88 ± 28	−244 ± 78	0.94 ± 0.30	0.77	SPT-CL 0528−5300

Notes.
[a] The error simply reflects the S/N with no systematic uncertainty included.
[b] Temperature decrement value with the effect of the ACT beam deconvolved $\delta T_0 \times C^{-1}(\theta_c)$.
[c] Provided for reference: see Menanteau et al. (2010) for the sources of redshifts.
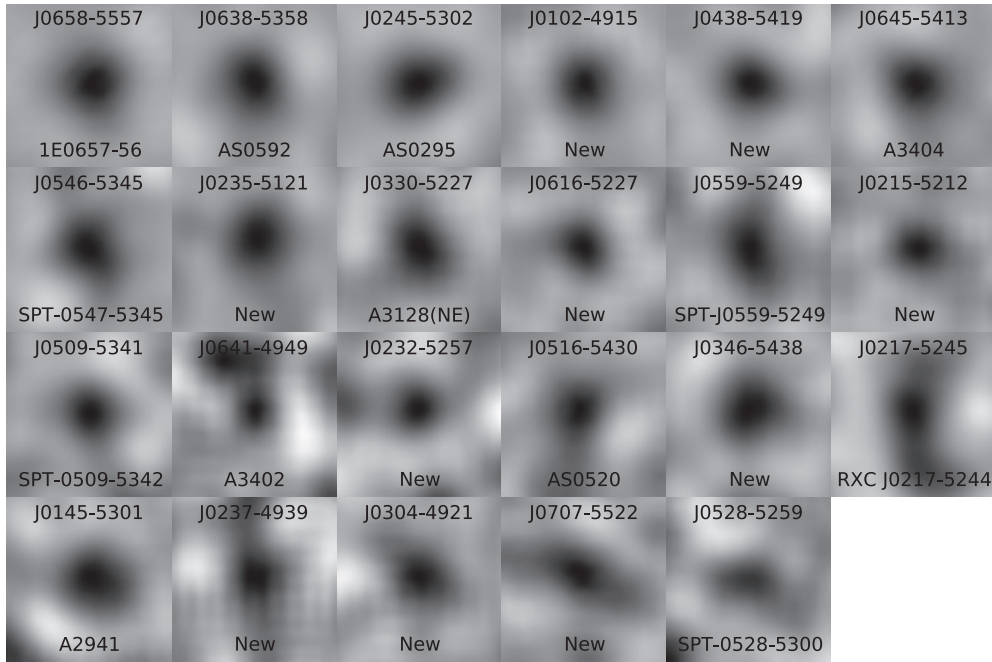
Figure 3. Temperature decrements at 148 GHz of 23 clusters. Each thumbnail is approximately 8' on a side and is excised from the source-removed, filtered map. The gray scale of each thumbnail is symmetric about zero with a range set to the depth of the decrement. The ordering of the clusters is according to decreasing S/N from left to right and top to bottom. The structure northeast of ACT-CL J0641−4949 may be part of the cluster or may be contamination: the decrement of this nearby cluster may be noise boosted. ACT designations are at the top of each thumbnail and alternate names at the bottom, denoted "New" if newly discovered by ACT.
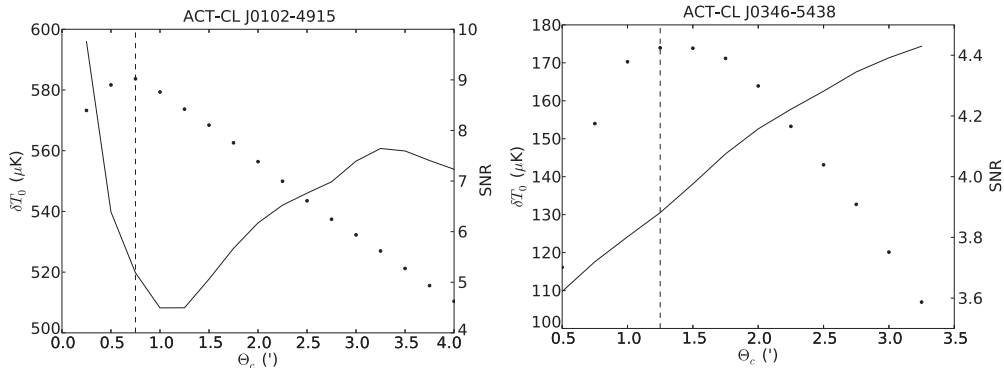
Figure 4. Decrement amplitude and S/N vs. the filter core radius for two newly discovered clusters. The solid curve corresponds to the decrement while the dotted curve corresponds to the S/N. A vertical dashed line marks the maximum S/N identified by the extraction algorithm.

shown to be $\sqrt{S/N^2 - 3}$. In the case of S/N = 4, therefore, the optimization over location and core radius increases the raw decrement estimate by 10% on average.

Decrement measurements at 150 GHz have been published for a number of the known clusters in the current ACT sample. Halverson et al. (2009), using the Atacama Pathfinder Experiment telescope, reported a decrement for the Bullet Cluster of -771 ± 71 μK while Plagge et al. (2010), using the SPT, reported -932 ± 43 μK. Plagge et al. (2010) also found decrements for AS0520 (-217 μK), A3404 (-472 μK), AS0592 (-529 μK), and RXC J0217.2−5244 (-217 μK), all of which are in reasonable agreement with the $\delta T'_0$ values in Table 1. The central values of the SPT estimates are, however, systematically more negative than the central values reported in Table 1.

Table 1 also contains the central Compton y parameter y'_0, which is related to the central decrement $\delta T'_0$ by

$$\frac{\delta T'_0}{T_{\mathrm{CMB}}} = y'_0 \left(x \frac{e^x + 1}{e^x - 1} - 4 \right) (1 + \delta_{\mathrm{SZE}}(x, T_e)). \quad (3)$$

In this equation, $x = h\nu/k_B T_{\mathrm{CMB}}$ and T_e is the temperature of the electron gas. In this equation, we have omitted the $\sim$10% contribution of the kinetic SZ (kSZ) effect, which arises due to the peculiar velocity of the cluster (Sunyaev & Zel'dovich 1970). Because we do not know the bulk velocity of the clusters, we do not account for the contribution of the kinetic effect, which adds to the uncertainty in the derived y parameter. The y parameter itself is the product of the optical depth through the cluster and $k_B T_e/m_e c^2$ where m_e is the electron mass:

$$y'_0 = \frac{k_B T_e}{m_e c^2} \int n_e \sigma_T \, d\ell, \quad (4)$$

where σ_T is the Thomson cross section and isothermality of the cluster is assumed. The relativistic correction $\delta_{\mathrm{SZE}}(x, T_e)$ at 148 GHz varies from -0.03 to -0.10 for the ACT sample, corresponding to cluster temperatures in the range 5–15 keV (Nozawa et al. 2006). We have used X-ray temperatures tabulated in Menanteau et al. (2010) as inputs to the relativistic correction for a subset of the clusters. For clusters without an

X-ray temperature, we use a correction of -0.05, which roughly corresponds to a temperature of 7.5 keV, characteristic of our sample.

For all but one case, there is no obvious correlation of the cluster decrements with strong sources. The one exception is AS0295. Approximately $4'$ northeast of the cluster is ACT-S J024539$-$525756 (Marriage et al. 2011) with a 148 GHz flux density of 18.4 mJy (S/N = 7.6). The source is also identified at 0.84 GHz in the Sydney University Molonglo Sky Survey (SUMSS) catalog (Mauch et al. 2003). Therefore, the source flux density is most likely dominated by synchrotron emission. From simple geometric arguments, there is approximately a 10% chance that one of the ACT sources would randomly fall within $4'$ of one of the 23 clusters, so the source–cluster proximity may be a projection effect. Furthermore, the source's large angular displacement from the cluster implies that it is unlikely a lensed background galaxy. Finally, note that this source does not appear near AS0295 in Figure 3 because the source was removed from the data prior to filtering.

There are slight differences between the cluster properties as presented in Table 1 and in Menanteau et al. (2010). The S/N and, to a lesser degree, position differ due primarily to two facts. First, the data reduction (i.e., the map) used for Menanteau et al. (2010) was a preliminary version of that used for this work. The map used for this work corresponds to that used in Fowler et al. (2010) and Marriage et al. (2011). Second, the signal and noise terms used in the matched filter for the candidate selection in Menanteau et al. (2010) are different from those used in this study. These differences in analysis arose from the need to execute the optical follow-up before the ACT pipeline and cluster extraction algorithm were fully mature. The differences in S/N generally correspond to approximately 1σ fluctuations between the reductions.

4. SIMULATED PURITY AND COMPLETENESS

In order to assess the ratio of true detections to total detections (purity) and the fraction of clusters recovered (completeness), we run our filtering and extraction algorithm on simulations of the ACT data. The simulations were constructed using the millimeter signal (SZ, CMB, etc.) from Sehgal et al. (2010) and noise from ACT difference maps. In order to avoid confusion due to source–SZ correlations included in Sehgal et al. (2010), the source component of those simulations was not included. The undetected/unmasked sources in the data contribute a small fraction of the rms of the filtered map, which is dominated by white detector and photon shot noise (Marriage et al. 2011).

Although it is expected that, from a noise power perspective, omitting the sources in this study will not significantly impact the analysis, concern remains that millimeter sources may be correlated with clusters, either as cluster members or as lensed backgrounds. Studying 573 nearby clusters with 1.4 GHz data from the NRAO Very Large Array Sky Survey, Lin & Mohr (2007) found that the fraction of brightest cluster galaxies being radio loud is higher compared to that of cluster galaxies of similar luminosity. Extrapolating in frequency and redshift, this study concluded that roughly 10% of clusters may have 150 GHz decrements "filled in" by synchrotron emission from a resident active galactic nucleus. Marriage et al. (2011) included a cross comparison of the 150 GHz bright source population detected by ACT and the 23 REFLEX X-ray clusters (Böhringer et al. 2004) which fall within the survey area. The study cross-identified three clusters with 150 GHz sources. These three clusters were all at redshifts below $z = 0.06$ in contrast to
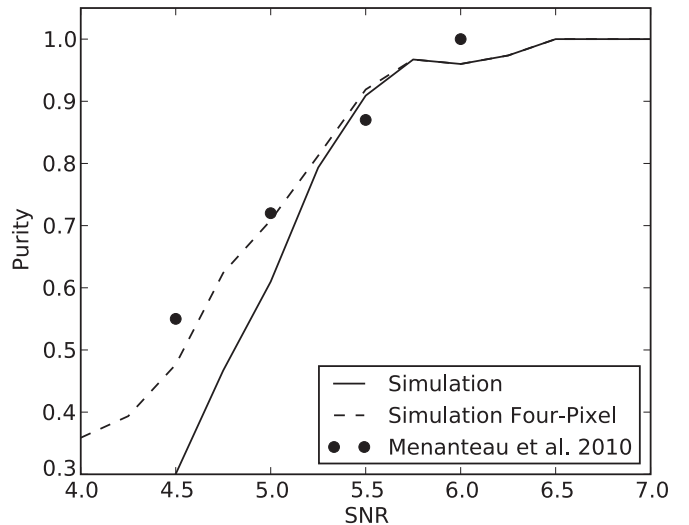

Figure 5. Simulated purity. Purity is defined as the fraction of true detections in the sample. The four-pixel candidate selection, which was used to produce the sample in Menanteau et al. (2010), requires cluster candidates to have at least four pixels with S/N > 4.0. The dashed line gives the simulated purity associated with the four-pixel selection function. The solid line is the purity function corresponding to a selection function based on the single highest S/N cluster pixel. As expected the four-pixel purity of the simulated sample is in reasonable agreement with that derived from optical follow-up of candidates from the data Menanteau et al. (2010). The sample is essentially pure at S/N > 6.

the higher redshift sample of this work. Lensed background dusty star-forming galaxies may also contaminate the SZ signal. Wilson et al. (2008) found a bright, lensed, dusty source at 1.1 mm behind the Bullet Cluster. Vieira et al. (2010) found that the lensed dusty population was characterized by maximum 150 GHz flux densities below the 5 mJy range. This finding is consistent with the Wilson et al. (2008) bright Bullet Cluster lensed source flux of 15.9 mJy at 1.1 mm ($\sim$4 mJy at 150 GHz assuming a spectral index of 2). Filtered at the characteristic scale ($0.\!'75$) of this work, such sources would produce a peak brightness of 10 μK. As the decrements in this work measure of order 100 μK, contributions from dusty sources may affect the purity and completeness of the faint end of the sample, but the bright end (S/N > 6) should be relatively immune to detection problems due to dusty sources.

In order to build simulated catalogs to compare with that from the data, we run the filtering and detection pipeline described in Section 2.2 on each of six simulations extracted from the Sehgal et al. (2010) sky. We identify decrements with clusters from the simulated catalog with $M_{500c} > 2 \times 10^{14}\ M_\odot$ and at redshifts $z > 0.1$. The identification radius is $3'$. This radius was chosen by studying significant decrements detected in the simulations and their offset from the position reported in the simulated catalog. By coincidence, this is also approximately the size of the optical fields of view used in the Menanteau et al. (2010) follow-up work. In nearly all cases, the arcminute-scale displacements resulted from extended non-spherical, often double-peaked, clusters. In these cases, it was easier for noise fluctuations to move the detection position away from the minimum of the cluster potential as reported in the catalogs from Sehgal et al. (2010).

Figure 5 shows the purity as derived from the simulations. In order to reproduce the original selection function from Menanteau et al. (2010), we require that a cluster candidate have four conjoined map pixels with S/N > 4.0. This requirement is
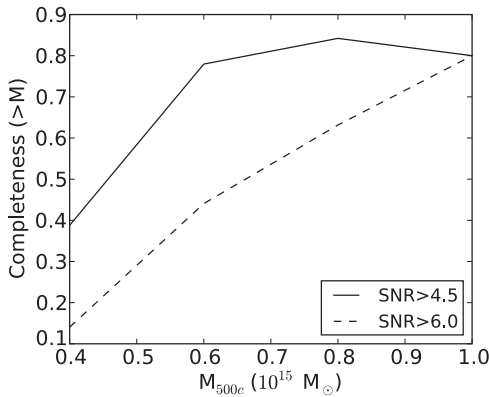
Figure 6. Cumulative completeness of the simulated sample. At $M_{500c} > 6 \times 10^{14} M_\odot$, the approximation to the total sample (S/N > 4.5) is ~80% complete. The completeness degrades at the edges of the map; taking the cleanest 230 deg^2 from Fowler et al. (2010), the completeness rises to 90%.

Table 2
Cluster Mass Estimates

ACT ID[a]	M_{500c}[b] $(\times 10^{14} M_\odot)$
ACT-CL J0102−4915	9.9 ± 3.5
ACT-CL J0235−5121	6.2 ± 1.4
ACT-CL J0245−5302	6.6 ± 1.0
ACT-CL J0330−5227	9.7 ± 1.7
ACT-CL J0438−5419	12.1 ± 2.2
ACT-CL J0546−5345	5.2 ± 2.2
ACT-CL J0559−5249	5.3 ± 1.5
ACT-CL J0616−5227	6.5 ± 1.6
ACT-CL J0638−5358	9.1 ± 0.6
ACT-CL J0645−5413	7.6 ± 0.6
ACT-CL J0658−5557	14.0 ± 1.2

Notes.
[a] This is a subset of clusters from Table 1 with S/N > 5.
[b] Masses derived from X-ray luminosities using the $M-L_X$ relation in Vikhlinin et al. (2009). The error only includes statistical error propagated from error on L_X.

intended to boost the purity of the sample with respect to a sample drawn with the requirement that only a single pixel have a high S/N. Figure 5 shows the purity versus S/N for both of these selection effects. As expected, the four-pixel requirement increases the purity as determined by the simulations. Furthermore, the four-pixel purity agrees reasonably well with the purity measured in Menanteau et al. (2010). The simulations imply that the purity of the sample with S/N > 6 is 95%, consistent with the finding that all these clusters have optical counterparts. Furthermore, both the four-pixel and single-pixel selection process yield the same purity for the high S/N sample. Below S/N = 6, simulations show that the four-pixel purity falls off in a manner consistent with the purity determined from the optical follow-up. The single-pixel purity falls significantly faster with decreasing S/N compared to that of the four-pixel or optically measured purity. We therefore choose the four-pixel selection function to evaluate the completeness of the sample below.

It is straightforward to simulate the cumulative completeness as a function of cluster mass for the pure population at S/N > 6. As shown in Figure 6 with the dashed curve, we count the simulated clusters above a given mass and detected at S/N > 6. We then divide the number of detected clusters by the total number of clusters in the same mass range. The resulting cumulative completeness shows that the high S/N sample is approximately ~45% complete for $M_{500c} > 6 \times 10^{14} M_\odot$ and rises to 80% complete for $M_{500c} > 1.0 \times 10^{15} M_\odot$. One reason for incompleteness among the high-mass population is that clusters at $z < 0.3$ are characterized by larger angular scales than their high-redshift counterparts and start blending with the fluctuations in the CMB. Dividing the simulated sample in redshift bins of $\delta z = 0.2$ bins between $z = 0.1$ and $z = 1.1$, the completeness of this sample, in the mass range $M_{500c} > 6 \times 10^{14} M_\odot$, increased smoothly from 30% complete in the lowest redshift bin ($z = 0.1-0.3$) to 70% complete in the highest bin ($z = 0.9-1.1$).

It is not so straightforward to reproduce the cumulative completeness function for the entire sample presented in Menanteau et al. (2010), which is based on a previous reduction of the data. As shown in Figure 13 of Menanteau et al. (2010), the follow-up observations were completed for a preliminary candidate list down to S/N = 4.2. Below S/N = 4.8, the follow-up was performed for a decreasing fraction of candidates such that, by S/N = 4.2, the fraction of the total candidates followed up was 50%. In order to approximately simulate the smoothly declining

selection function of the follow-up for candidates in the range S/N = 4.2–4.8, we simply introduce a hard cut at S/N = 4.5 where the sampling goes from 100% to 0%.

With this prescription for modeling the entire sample, the simulations suggest that ~80% of all clusters with $M_{500c} > 6 \times 10^{14} M_\odot$ are detected. Figure 6 shows the full cumulative completeness function with a solid curve. Unlike in the case of the high S/N sample discussed above, the simulations suggest that completeness of the full sample in the range $M_{500c} > 6 \times 10^{14} M_\odot$ is not a strong function of redshift ($z = 0.1-1.1$). Another important reason for the incompleteness is that a fraction of massive clusters are disturbed, showing elongated structure in the plane of the sky, and thus are not well matched to our β-model filter. Conversely, the simulations suggest our sample likely includes high-redshift relaxed, spherical clusters of lower mass (e.g., $4 \times 10^{14} M_\odot$). Another feature of the data which drives the overall completeness down is the high level of noise toward the edge of the map. If the region under consideration is restricted to the central 230 deg^2 used for the power spectrum study in Fowler et al. (2010), then the completeness estimate for clusters with $M_{500c} > 6 \times 10^{14} M_\odot$ increases to ~90%.

5. SZ–MASS CORRELATION

In this section, we perform a largely illustrative, preliminary study of the correlation of the SZ signal with mass for the more significant (S/N > 5) half of the SZ detections. For the SZ signal we use the central y'_0 as described in Section 3 and listed in Table 1. For the total mass, we derive M_{500c} using X-ray luminosities from Menanteau et al. (2010) and the L_x-M relation from Vikhlinin et al. (2009). For all clusters but A3128 (NE), the X-ray luminosities were derived from the *ROSAT* All Sky Survey. For A3128 (NE), the available higher resolution *Chandra* results from Menanteau et al. (2010) were used to help separate the flux from the more massive background cluster from the less massive cluster at low redshift (Werner et al. 2007). An additional scale factor of ~1.6 was needed to convert the luminosities from the 0.1–2.4 keV band in Menanteau et al. (2010) to the 0.5–2.0 keV band required by the correlation in Vikhlinin et al. (2009). The resulting M_{500c} estimates are shown in Table 2. The error given for M_{500c} only includes statistical
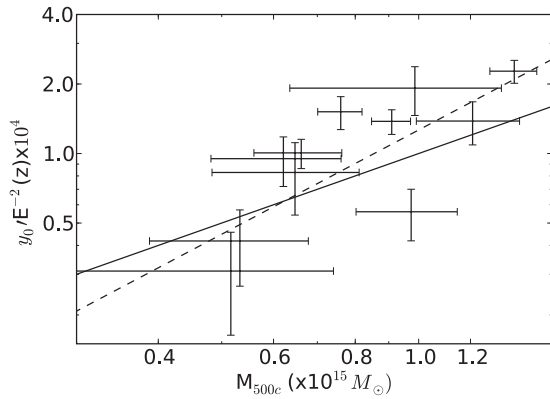
Figure 7. SZ–mass correlation. Estimated Compton y parameter estimates (Table 1) are plotted, scaled for self-similar evolution, against X-ray luminosity-derived mass estimates (Table 2) for the more significant half (S/N > 5) of the cluster sample. The line plotted is the self-similar model $y_0' \propto M E^2(z)$ (see the Appendix). The model, which is not fit to the data, agrees reasonably well with the ACT data. For comparison, the dashed line shows a simulation-motivated model with logarithmic slope 3/2 (Motl et al. 2005).

error propagated from error on L_X. Additional scatter about this relation was measured to be 48% (Vikhlinin et al. 2009). Due to evolution and non-trivial processes in the ICM as well as the ongoing optical and X-ray follow-up of the ACT cluster sample will improve these mass estimates in the near future.

For self-similar evolution, the central y_0' is expected to scale as $M E^2(z)$ where $E^2(z) = \Omega_M(1 + z)^3 + \Omega_\Lambda$ for a flat ΛCDM universe. The conventional argument behind this scaling is given in the Appendix. Anticipating such a scaling, in Figure 7 we plot y_0' values scaled by $E^{-2}(z)$ against their corresponding M_{500c} estimates. Values used for Ω_M and Ω_Λ are 0.26 and 0.74, respectively (Komatsu et al. 2011). The errors plotted for y_0' are purely statistical. As discussed in Section 3, systematic errors, primarily due to uncertainty in the core radius, would increase the errors on y_0' by at least 20%. Because of systematic uncertainties associated with the estimators for y_0' and M_{500c}, no attempt has been made to fit scaling relations to these data. Given this precaution, however, the data appear consistent with the self-similar model plotted as a solid line in the figure. An additional dashed line with $y_0' \propto M^{3/2} E^2(z)$ approximates the y_0–M relation from numerical simulations including star formation and supernova feedback from Motl et al. (2005). The data also appear consistent with this model.

The SZ-mass relation presented here is for illustrative purposes using central y parameter estimates and a mass proxy that are available now for all clusters but which have a large scatter. The SZ signal estimate will be improved in future analyses using additional ACT bands as well as additional information on cluster gas and temperature profiles from the X-ray (e.g., Andersson et al. 2011). The precise relationship between the SZ signal and mass needs to be determined from more precise mass proxies such as X-ray temperature, galaxy velocity dispersion, and weak lensing. This work is in progress and will be reported in future publications.

6. CONCLUSION

ACT has identified the SZ signatures of 23 optically confirmed galaxy clusters at a frequency of 148 GHz in data taken during the 2008 observing season. Of these clusters, 10 are new discoveries. Together, ACT and SPT have reported 25 newly discovered systems. The *Planck* satellite will soon add its

complementary detections to the growing sample of SZ cluster discoveries. Due to the unique nature of the SZ effect, the sample is biased toward high-mass clusters at high redshifts. As such the sample complements current X-ray and optically selected catalogs. Among the clusters discovered by ACT, ACT-CL J0102−4915 stands out as a high-redshift cluster having an SZ temperature decrement comparable to that of the most massive known clusters. Purity estimates from simulations of the cluster extraction agree with the sample purity derived from optical follow-up in Menanteau et al. (2010). The simulations also estimate completeness of the sample at roughly 80% for $M_{500c} > 6 \times 10^{14} M_\odot$. Over the same mass range, the completeness increases to greater than 90% if only the lowest noise half of the survey area is considered. A comparison of the clusters' central Compton y parameters with X-ray luminosity-derived masses is in agreement with both self-similar scaling and scalings based on simulations that include star formation and supernova feedback.

Future work with the SZ effect from galaxy clusters will include ACT data from multiple seasons and multiple millimeter bands. In addition to the southern survey described in this work, ACT is also surveying the celestial equator to complement extant and future multifrequency cluster work in this highly accessible strip of sky.

APPENDIX

SELF-SIMILAR SCALING RELATION FOR y_0–M

Assuming an isothermal ICM and taking R as the radius of the cluster, the central Compton y parameter is proportional to the product of the electron temperature (T), average central electron number density (n_0), and R:

$$y_0 \propto n_0 T R. \tag{A1}$$

The electron density can be related through a mean molecular weight to the gas density which, assuming a standard gas fraction, can in turn be related to the total density (ρ) of dark matter plus gas. The total density is referenced to the background critical density ($\rho \propto \rho_c$), which evolves with redshift as $E^2(z) = \Omega_M(1+z)^3 + \Omega_\Lambda$ in a flat ΛCDM universe. Furthermore, the cluster radius is a function of the mass and density such that

$$R \propto \left(\frac{M}{\rho}\right)^{1/3} \propto \left(\frac{M}{E^2(z)}\right)^{1/3}. \tag{A2}$$

Under the assumptions of virialization and hydrostatic equilibrium, the temperature can be related to M and $E(z)$ (e.g., Bryan & Norman 1998):

$$T \propto M^{2/3} E^{2/3}(z). \tag{A3}$$

Combining these relations, the central Compton y parameter is seen to scale with mass and redshift as

$$y_0 \propto M E^2(z). \tag{A4}$$

REFERENCES

Andersson, K., et al. 2011, ApJ, in press, arXiv:1006.3068
Arnaud, M., Pratt, G. W., Piffaretti, R., Boehringer, H., Croston, J. H., & Pointecouteau, E. 2010, A&A, 517, A92
Bartlett, J. G., & Silk, J. 1994, ApJ, 423, 12
Benson, B. A., Church, S. E., Ade, P. A. R., Bock, J. J., Ganga, K. M., Henson, C. N., & Thompson, K. L. 2004, ApJ, 617, 829
Bernstein, J., & Dodelson, S. 1990, Phys. Rev. D, 41, 354
Birkinshaw, M. 1991, in Physical Cosmology, ed. A. Blanchard, L. Celnikier, M. Lachieze Rey, & J. Tran Thanh Van (Gif-sur-Yvette: Editions Frontieres), 177
Birkinshaw, M. 1999, Phys. Rep., 310, 97
Birkinshaw, M., Hughes, J. P., & Arnaud, K. A. 1991, ApJ, 379, 466
Bonamente, M., Joy, M., LaRoque, S. J., Carlstrom, J. E., Nagai, D., & Marrone, D. P. 2008, ApJ, 675, 106
Bonamente, M., Joy, M. K., LaRoque, S. J., Carlstrom, J. E., Reese, E. D., & Dawson, K. S. 2006, ApJ, 647, 25
Böhringer, H., et al. 2004, A&A, 425, 367
Bryan, G. L., & Norman, M. L. 1998, ApJ, 495, 80
Carlstrom, J. E., Holder, G. P., & Reese, E. D. 2002, ARA&A, 40, 643
Carlstrom, J. E., Joy, M., & Grego, L. 1996, ApJ, 456, L75

Carlstrom, J. E., et al. 2011, PASP, 123, 568
Culverhouse, T. L., et al. 2010, ApJ, 723, L78
Das, S., et al. 2011, ApJ, 729, 62
Dunkley, J., et al. 2011, ApJ, in press, arXiv:1009.0866
Fowler, J. W., et al. 2007, Appl. Opt., 46, 3444
Fowler, J. W., et al. 2010, ApJ, 722, 1148
Francis, M. R., Bean, R., & Kosowsky, A. 2005, J. Cosmol. Astropart. Phys., JCAP12(2005)001
Freedman, W. L., et al. 2001, ApJ, 553, 47
Haehnelt, M. G., & Tegmark, M. 1996, MNRAS, 279, 545
Haiman, Z., Mohr, J. J., & Holder, G. P. 2001, ApJ, 553, 545
Hajian, A., et al. 2011, ApJ, in press, arXiv:1009.0777
Halverson, N. W., et al. 2009, ApJ, 701, 42
Herbig, T., Lawrence, C. R., Readhead, A. C. S., & Gulkis, S. 1995, ApJ, 449, L5
Herranz, D., Sanz, J. L., Barreiro, R. B., Hobson, M., Martinez-Gonzalez, E., & Diego, J. M. 2002, Proc. SPIE, 4847, 50
Hicken, M., Wood-Vasey, W. M., Blondin, S., Challis, P., Jha, S., Kelly, P. L., Rest, A., & Kirshner, R. P. 2009, ApJ, 700, 1097
High, F. W., et al. 2010, ApJ, 723, 1736
Hincks, A. D., et al. 2010, ApJS, 191, 423
Holder, G. P., Mohr, J. J., Carlstrom, J. E., Evrard, A. E., & Leitch, E. M. 2000, ApJ, 544, 629
Holzapfel, W. L., et al. 1997, ApJ, 480, 449
Huang, C., et al. 2010, ApJ, 716, 758
Jones, M., et al. 1993, Nature, 365, 320
Komatsu, E., Kitayama, T., Suto, Y., Hattori, M., Kawabe, R., Matsuo, H., Schindler, S., & Yoshikawa, K. 1999, ApJ, 516, L1
Komatsu, E., et al. 2001, PASJ, 53, 57
Komatsu, E., et al. 2011, ApJS, 192, 18
Lin, Y., & Mohr, J. J. 2007, ApJS, 170, 71
Majumdar, S., & Mohr, J. J. 2004, ApJ, 613, 41
Mantz, A., Allen, S. W., Rapetti, D., & Ebeling, H. 2010, MNRAS, 406, 1759
Marriage, T. A., et al. 2011, ApJ, 731, 100
Marrone, D. P., et al. 2009, ApJ, 701, L114
Mason, B. S., et al. 2010, ApJ, 716, 739
Mauch, T., Murphy, T., Buttery, H. J., Curran, J., Hunstead, R. W., Piestrzynski, B., Robertson, J. G., & Sadler, E. M. 2003, MNRAS, 342, 1117
McInnes, R. N., Menanteau, F., Heavens, A. F., Hughes, J. P., Jimenez, R., Massey, R., Simon, P., & Taylor, A. 2009, MNRAS, 399, L84
Melin, J., Bartlett, J. G., & Delabrouille, J. 2006, A&A, 459, 341
Melin, J., Bartlett, J. G., Delabrouille, J., Arnaud, M., Piffaretti, R., & Pratt, G. W. 2011, A&A, 525, A139
Menanteau, F., et al. 2010, ApJ, 723, 1523
Motl, P. M., Hallman, E. J., Burns, J. O., & Norman, M. L. 2005, ApJ, 623, L63
Mroczkowski, T., et al. 2009, ApJ, 694, 1034
Murphy, T., et al. 2010, MNRAS, 402, 2403
Myers, S. T., Baker, J. E., Readhead, A. C. S., Leitch, E. M., & Herbig, T. 1997, ApJ, 485, 1
Nolta, M. R., et al. 2009, ApJS, 180, 296
Nozawa, S., Itoh, N., Suda, Y., & Ohhata, Y. 2006, Nuovo Cimento B, 121, 487
Plagge, T., et al. 2010, ApJ, 716, 1118
Press, W. H., Teukolsky, S. A., Vetterling, W. T., & Flannery, B. P. 1992, Numerical Recipes in C: The Art of Scientific Computing (2nd ed.; Cambridge: Cambridge Univ. Press)
Reese, E. D., Carlstrom, J. E., Joy, M., Mohr, J. J., Grego, L., & Holzapfel, W. L. 2002, ApJ, 581, 53
Rephaeli, Y. 1995, ApJ, 445, 33
Riess, A. G., et al. 2009, ApJ, 699, 539
Rozo, E., et al. 2010, ApJ, 708, 645
Sehgal, N., et al. 2010, ApJ, 709, 920
Sehgal, N., et al. 2011, ApJ, 732, 44
Staniszewski, Z., et al. 2009, ApJ, 701, 32
Sunyaev, R. A., & Zel'dovich, Y. B. 1970, Comments Astrophys. Space Phys., 2, 66
Swetz, D. S., et al. 2011, ApJS, 194, 41
Vanderlinde, K., et al. 2010, ApJ, 722, 1180
Vieira, J. D., et al. 2010, ApJ, 719, 763
Vikhlinin, A., et al. 2009, ApJ, 692, 1060
Werner, N., Churazov, E., Finoguenov, A., Markevitch, M., Burenin, R., Kaastra, J. S., & Böhringer, H. 2007, A&A, 474, 707
Wilson, G. W., et al. 2008, MNRAS, 390, 1061
Zel'dovich, Y. B., & Sunyaev, R. A. 1969, Ap&SS, 4, 301